



Published in final edited form as:

*Mol Imaging Biol.* 2018 August ; 20(4): 575–583. doi:10.1007/s11307-018-1164-4.

## Preliminary Results that Assess Metformin Treatment in a Preclinical Model of Pancreatic Cancer Using Simultaneous [<sup>18</sup>F]FDG PET and acidoCEST MRI

Joshua M. Goldenberg<sup>1,2</sup>, Julio Cárdenas-Rodríguez<sup>3</sup>, and Mark D. Pagel<sup>2</sup>

<sup>1</sup>Department of Pharmaceutical Sciences, The University of Arizona, Tucson, AZ, 85721, USA

<sup>2</sup>Department of Cancer Systems Imaging, The University of Texas M.D. Anderson Cancer Center, 3SCR4.3642, Unit 1907, Houston, TX, 77054-1901, USA

<sup>3</sup>Banner – University Medical Center, The University of Arizona, Tucson, AZ, 85724, USA

### Abstract

**Purpose**—We sought to determine if the synergy between evaluations of glucose uptake in tumors and extracellular tumor acidosis measured with simultaneous positron emission tomography (PET)/magnetic resonance imaging (MRI) can improve longitudinal evaluations of the response to metformin treatment.

**Procedures**—A standard 2-deoxy-2-[<sup>18</sup>F]fluoro-D-glucose ([<sup>18</sup>F]FDG) PET protocol that evaluates glucose uptake in tumors, and a standard acidoCEST MRI protocol that measures extracellular pH (pHe) in tumors, were simultaneously performed to assess eight vehicle-treated (control) mice and eight metformin-treated mice 1 day before treatment, 1 day after initiating daily treatment with metformin, and 7 days after initiating treatment. Longitudinal changes in SUV<sub>max</sub> and extracellular pH (pHe) were evaluated for each treatment group, and differences in SUV<sub>max</sub> and pHe between metformin-treated and control groups were also evaluated.

**Results**—MRI acquisition protocols had little effect on the PET count rate, and the PET instrumentation had little effect on image contrast during acidoCEST MRI, verifying that [<sup>18</sup>F]FDG PET and acidoCEST MRI can be performed simultaneously. The average SUV<sub>max</sub> of the tumor model had a significant decrease after 7 days of treatment with metformin, as expected. The average tumor pHe decreased after 7 days of metformin treatment, which reflected the inhibition of the consumption of cytosolic lactic acid caused by metformin. However, the average SUV<sub>max</sub> of the tumor model was not significantly different between the metformin-treated and control groups after 7 days of treatment, and average pHe was also not significantly different between these groups. For comparison, the combination of average SUV<sub>max</sub> and pHe measurements significantly differed between the treatment group and control group on Day 7.

---

Correspondence to: Mark Pagel; [mdpapel@mdanderson.org](mailto:mdpapel@mdanderson.org).

Electronic supplementary material The online version of this article (<https://doi.org/10.1007/s11307-018-1164-4>) contains supplementary material, which is available to authorized users.

Compliance with Ethical Standards

Conflict of Interest

The authors declare that they have no conflict of interest.

**Conclusions**— $^{18}\text{F}$ FDG PET and acidoCEST MRI studies can be performed simultaneously. The synergistic combination of assessing glucose uptake and tumor acidosis can improve differentiation of a drug-treated group from a control group during drug treatment of a tumor model.

### Keywords

$^{18}\text{F}$ FDG PET; acidoCEST MRI; PET/MRI; Metformin

---

### Introduction

Molecular imaging of cancer has often exploited the dysregulated metabolism of solid tumors. For example, 2-deoxy-2- $^{18}\text{F}$ fluoro-D-glucose ( $^{18}\text{F}$ FDG) is commonly administered to patients, which accumulates in tumor cells that have upregulated glucose transport to feed a variety of metabolic processes including glycolysis [1]. Positron emission tomography (PET) is then used to detect the localized accumulation of  $^{18}\text{F}$ FDG to identify viable regions of a primary tumor, as well as viable metastases. Furthermore,  $^{18}\text{F}$ FDG PET is used to monitor a general decrease in tumor metabolism in response to anti-cancer treatment, both in patients undergoing treatment and in small animal tumor models tested with experimental therapeutics [2, 3].

As another example of imaging tumor metabolism, the extracellular pH (pHe) of the tumor microenvironment can be measured using chemical exchange saturation transfer (CEST) magnetic resonance imaging (MRI) [4]. We have developed a version of this molecular imaging technique to monitor tumor glycolysis that causes lactic acid production and secretion, which is known as acidoCEST MRI [5–7]. Other researchers have developed similar CEST MRI methods that have been used to measure pHe in tumors, kidneys, and bladder, which further demonstrates the feasibility of this MRI technique [8–12]. Using these methods, tumors with faster growth rates have been shown to have lower pHe values, indicating that tumor pHe is a biomarker for tumor viability that may compliment  $^{18}\text{F}$ FDG PET studies [5]. Also, these CEST MRI methods have shown that tumor pHe can significantly increase in response to drugs that generally decrease tumor metabolism, which may also compliment  $^{18}\text{F}$ FDG PET studies [13]. Similarly, these methods have measured an increase in tumor pHe in response to an inhibitor of the lactic acid production pathway [14, 15], and a decrease in tumor pHe in response to a mitochondrial poison that redirects glucose metabolism towards glycolysis and lactic acid production [16]. These latter studies suggest that acidoCEST MRI can provide new insights into changes in tumor metabolism that can further compliment  $^{18}\text{F}$ FDG PET studies when evaluating drug response in tumors.

AcidoCEST MRI detects two CEST signals from two types of amide protons on iopamidol (Isovue®, Bracco Imaging SpA, Milan, Italy), a CT agent that has been repurposed for our MRI studies (Fig. 1a) [17, 18]. Selective radio frequency saturation of the MR resonance frequency of an amide proton causes the MR signal of the respective proton to disappear. Chemical exchange between a saturated proton and a proton on a water molecule transfers the saturation to water, causing the MR signal of water to decrease (Fig. 1c–f) [19]. The

chemical exchange rate of each type of amide proton on iopamidol has different dependencies on pH, so that an analysis of the CEST effects from both amide protons can measure pH [7]. In practice, the saturation frequency is iterated among many values to generate a CEST spectrum that is analyzed to measure pH (Fig. 1b). In addition, CEST is an insensitive imaging technique, requiring signal averaging to produce high-quality results. CEST images are acquired before and after administration of the contrast agent, so that the difference between the images can be used to remove the effects of endogenous CEST contrast from the analysis of the exogenous agent. These many multi-second image acquisitions typically require a lengthy ~ 35 min to complete, and additional time to optimize imaging conditions can cause acidoCEST MRI scan to take ~ 45 min to perform. This lengthy scan time limits opportunities to append additional molecular imaging methods to the scan session, such as performing a [ $^{18}\text{F}$ ]FDG PET scan before or after an acidoCEST MRI scan.

To address this practical limitation, instrumentation has been developed to perform simultaneous PET/MRI studies [20]. A PET detector can be inserted into an MRI magnet, providing the opportunity to independently perform PET and MRI studies without loss in image quality from each modality. We sought to investigate whether a PET/MRI system could provide a practical platform for performing simultaneous [ $^{18}\text{F}$ ]FDG PET and acidoCEST MRI studies. In addition, we investigated whether results from [ $^{18}\text{F}$ ]FDG PET and acidoCEST MRI studies could be combined to improve the evaluation of the early response in a tumor model undergoing drug treatment.

## Materials and Methods

### PET/MRI System

Simultaneous PET/MRI studies were facilitated by using a NuPET<sup>TM</sup> PET imaging system (Cubresa, Inc., Winnipeg, MB, Canada) and a 7T Biospec MR imaging system (Bruker Biospec, Inc., Billerica, MA) [21]. A cylindrical, quadrature MR transceiver volume coil (Bruker Biospec, Inc.) with a 35 mm inner diameter and 55 mm outer diameter was placed inside a 5-mm-thick plastic sleeve, which was then placed in a cylindrical NuPET<sup>TM</sup> detector that had a 60 mm inner diameter and a 114 mm outer diameter. The axial centers of the MRI coil and PET detector system were aligned within 1 mm. The transverse axes of each detector were also approximately aligned, and further alignment of PET and MR images was performed with rigid rotation of the transverse images using VivoQuant v3.0 (INVICRO, Inc., Boston, MA). Then this assembly was placed inside the 20-cm cylindrical magnet bore, which contained a cylindrical B-GA 12S gradient coil with a 114 mm inner diameter and 198 mm outer diameter. The axial centers of the detector were aligned with the axial center of the bore within 1 mm.

To test this configuration, we compared the PET count rates acquired with [ $^{18}\text{F}$ ]FDG in saline that had activities between 2 and 35 MBq with no MR acquisition and while acquiring fast low angle shot (FLASH), rapid acquisition with relaxation enhancement (RARE), echo planar imaging (EPI), and CEST fast imaging with steady state precession (FISP) MRI acquisition sequences. We also compared MR images with these acquisition methods with and without the NuPET<sup>TM</sup> system in the magnet bore. MR images were acquired at room

temperature using 20 tubes with 3 mm inner diameters and 5 mm outer diameters, each filled with 0.5 mM Gd-DOTA (Dotarem, Gubert LLC, Bloomington, IN) to reduce the  $T_1$  relaxation time constant to 0.4 s and allow the imaging session to be performed more rapidly. Measurements of the signal-to-noise ratio (SNR) were performed at the center of the coil, by measuring the standard deviation of the image area that did not represent a sample, and measuring signal from an image area that represented a sample at + 2.0 and – 2.0 cm from the center along the axial dimension, and + 1.0 and – 1.0 cm along the orthogonal transverse axes, for a total of seven measurements. In addition, the contrast-to-noise ratio (CNR) was evaluated for the CEST-FISP MRI protocol with and without the NuPET™ system, because CEST is a measure of relative MRI contrast rather than absolute MRI signal. The CNR measurements were obtained by comparing the MR signal of a sample without and with selective saturation applied at 10 ppm.

### Tumor Model

All mice were cared for in compliance with protocols approved by the Institutional Animal Care and Use Committee of the University of Arizona. MIA PaCa-2 human pancreatic ductal adenocarcinoma cells were prepared by trypsinization, rinsing once in phosphate buffered saline (PBS), and suspended in 50 % Matrigel™ (BD Biosciences, Franklin Lakes, NJ, USA) and 50 % PBS. Sixteen female SCID (6–8 weeks old) mice purchased from the Jackson Laboratory (Bar Harbor, ME, USA), approximately 20 g each, were injected subcutaneously in the right flank with  $10^7$  cells in 0.1 ml of saline. Tumor volume measurements were performed using a caliper every 2 days, calculated as  $\pi/6 \times (\text{short axis})^2 \times (\text{long axis})$ . Tumors grew for 21 days to a minimum volume of 300 mm<sup>3</sup> before initiating PET/MRI studies. We designed the study with substantially large tumors so that tumors remained constant for 3 days before acquiring images, to provide some assurance that the tumors were physiologically stable.

Mice were fasted for at least 5 h prior to PET/MRI scans. After obtaining PET/MR images on day –1 (relative to initiating treatment on day 0), seven mice were treated with 350 mg/Kg metformin in 100  $\mu$ l of 0.9 % saline administered intraperitoneally daily for 8 days. Another seven mice were treated with 100  $\mu$ l of 0.9 % saline without metformin, also administered intraperitoneally daily for 8 days. PET/MR images were also acquired on day 1 and day 7. One mouse per group expired after initiating treatment on day 0 and before imaging on day 1. Two mice in the control group were not imaged on day 1 and day 7 due to limited availability of [<sup>18</sup>F]FDG. After the last PET/MRI scan, each mouse was euthanized by cervical dislocation.

### In vivo PET

[<sup>18</sup>F]FDG was purchased from PET Net Pharmaceuticals (Phoenix, AZ, USA). The activity of the [<sup>18</sup>F]FDG was measured using an Atomlab 300 dosimeter (Biodex Medical Systems, Inc., Shirley, NY, USA). The [<sup>18</sup>F]FDG was diluted with 0.9 % saline to prepare a sample with 4–12 MBq (0.1–0.32 mCi) in 250  $\mu$ l total volume. This sample was intravenously injected into a mouse under 1.5 % isoflurane anesthesia in O<sub>2</sub> carrier gas (Fig. 2). Anesthesia was removed from the mouse for 45 min to improve tracer uptake into the tumor. The mouse was then prepared for PET/MR imaging by re-anesthetizing the mouse with 1.5–

2.5 % isoflurane in O<sub>2</sub> carrier gas, placing a 27 G catheter in the tail vein, and inserting the mouse into the PET/MRI system. The flank tumor was positioned to be at the axial center of the MRI and PET detectors. To obtain PET images, a 1 min localizer PET scan was performed to center the mouse within the detectors. Then a PET image was acquired with a 6.4 × 6.4 cm<sup>2</sup> FOV for 56 min, while MR images were simultaneously acquired as described below. During the scan session, physiologic respiration rate and core body temperature of the mouse were monitored while maintaining their temperature at 37.0 ± 0.2 °C using warm air controlled by a temperature feedback system (SA Instruments, New York, USA). After the PET/MRI scan session, the mouse was removed from the PET/MRI system and allowed to recover.

### In vivo MR Imaging

We performed a RARE MRI acquisition to localize the flank tumor, which required 3.1 min to acquire. AcidoCEST MRI studies were performed with a CEST-FISP MRI acquisition protocol using a 3.7 ms TR; 1.6 ms TE; 1 average; 15° excitation pulse angle; 1.0-mm slice thickness; 6.4 cm<sup>2</sup> FOV; 128 × 128 matrix; 0.5 mm<sup>2</sup> in-plane resolution; centric encoding order; unbalanced “FID” mode; 393 ms scan time [22]. The saturation period that preceded each FISP acquisition consisted of 3.0 μT saturation power and a 3.0 s continuous wave radio frequency pulse with no additional spoiling, fat saturation pulses or respiration gating. Selective saturation was applied at 40 frequencies ranging from -11 to -3 ppm in 2 ppm increments; -2.5 to 2.5 ppm in 0.5 ppm increments; 2.7 to 9 ppm in 0.3 ppm increments; and at 10 and 11 ppm. This series of 40 CEST images was acquired four times for a total scan time of 13 min. Then 200 μl of 370 mg/ml (976 mM) iopamidol was administered through the tail vein catheter. Iopamidol was then infused *via* the catheter at 400 μl/h for the remainder of the MRI scan session. Six post-injection acidoCEST MRI scans were conducted in a total scan time of 23 min.

### Image Processing

The 3D PET image was reconstructed using Ordered Subset Maximum *A Posteriori* One-Step Late (OSMAPOSL) iterative algorithm to provide 0.64 × 0.64 × 1.0 mm resolution. The mean activity in the tumor was measured using VivoQuant v3.0, and was normalized by the time-corrected injected dose and mouse body weight to produce a measurement of SUV<sub>max</sub>.

CEST MR images were analyzed on a pixelwise basis using customized software developed with MATLAB R2016b (MathWorks, Inc., Natick, MA) [7]. For each mouse, the average of four pre-injection and six post-injection MR images were spatially smoothed with Gaussian filtering. The pre-injection image was subtracted from the post-injection image at each saturation frequency, which removed static CEST image contrast before and after injection of the agent. The difference images were used to construct a CEST spectrum for each pixel of the tumor. The Bloch-McConnell equations modified to include pHe as a fitting parameter were fit to each CEST spectrum. This analysis estimated the pHe and concentration of agent in each pixel. The average of the pixelwise pH and concentration values were determined for each tumor. Although a similar process could have generated a single CEST spectrum of the

region-of-interest in the tumor, the pixelwise analysis can more easily reduce the effects of  $B_0$  and  $B_1$  inhomogeneity throughout the tumor when estimating concentration and pHe [6].

### Statistical Analysis

A Student's  $t$  test assuming two tails and equal variances was used to evaluate the statistical significance of the average change in  $SUV_{max}$  from day  $-1$  to day 1 or day 7 for the treated group, and the same changes in  $SUV_{max}$  for the control group. The same tests were performed to evaluate average changes in pHe and concentration of the agent. A Student's  $t$  test was also used to evaluate differences in the treated *vs.* control groups for  $SUV_{max}$ , pHe, or concentration on day  $-1$ , 1, or 7. In a separate analysis, a Hotelling's  $T^2$  distribution test was used to evaluate the combination of  $SUV_{max}$  and pHe for the same relationships listed above.

### Results

The MRI transceiver coil fit snugly within the NuPET™ detector, and the NuPET™ detector fit snugly within the magnet bore with the gradient system, which facilitated alignment of the coils. A comparison of PET and MR images verified that the axial centers of each coil matched within 1 mm, which is the spatial resolution of the PET images. The 3D PET image volume was easily aligned with the 2D MR image by rigid rotation about the longitudinal axis of the images.

The PET count rates while performing MRI acquisitions were within 2 % of PET count rates without performing MRI acquisitions, indicating that PET acquisitions were not affected by MRI acquisitions even during fast MR gradient switching or long selective saturation pulses. This result agreed with previous PET assessments of this technology [23]. The SNR of spin-echo and gradient echo MR images with the NuPET™ insert were within 97–101 % of the SNR without the insert, with a standard deviation of 2.3–3.4 % among the seven measurements made with each MR imaging protocol. In addition, the NuPET™ insert did not create artifacts or spatial distortions that were visible in the MR images. The SNR of the EPI and CEST-FISP MR images with the NuPET™ insert were 89 and 88 % of the SNR without the insert, demonstrating a minor signal loss for MR protocols with fast gradient switching during acquisition. This result agreed with previous MRI assessments of this technology [24]. However, the CEST-FISP MR images with the PET insert had a CNR that was 96 % of the CNR without the PET insert, demonstrating that the PET insert only has a minor effect on CEST-FISP MRI studies. Furthermore, acidoCEST MRI relies on the ratio of CEST signals generated from two types of amide protons on iopamidol. Decreasing the CEST signals from each amide proton by the same percentage does not affect this ratio of CEST signals, or the widths of the features in the CEST spectrum, and therefore does not impact the measurement of pH with acidoCEST MRI [25]. Overall, these studies verified that both [ $^{18}\text{F}$ ]FDG PET and acidoCEST MRI could be performed simultaneously.

The PET/MRI system successfully produced CEST spectra with good CNR (Fig. 3a, b, Figs. S1–S3).

The CEST signal from the proton at 5.6 ppm is stronger at lower pHe relative to the signal from the proton at 4.2 ppm, while the CEST signal from the proton at 4.2 ppm is stronger at higher pHe. Bloch fitting of the relative amplitudes as well as the widths of the features in the CEST spectrum are largely responsible for estimating pHe (Fig. 3c, d, Figs. S1–S3) [7, 26]. For comparison, the absolute magnitudes of both CEST signals at 5.6 and 4.2 ppm are dependent on concentration, so that Bloch fitting of the magnitude of the CEST spectrum is largely responsible for estimating concentration. This result shows that pHe and concentration can both be estimated from Bloch fitting in a largely independent manner. Our Bloch fitting method for analyzing CEST spectra was used to create pixelwise parametric maps of pHe and agent concentration in each tumor, which were compared to corresponding parametric maps of  $SUV_{max}$  from PET imaging (Fig. 4a–d, Figs. S4–S6).

We first evaluated the changes in  $SUV_{max}$  or pHe as individual imaging biomarkers, using a One Sample Student's *t* test. A significant decrease in  $SUV_{max}$  was observed between day –1 and day 7 in the group of mice treated with metformin (Fig. 5a). Similarly, a significant decrease in pHe was observed between the same days for this treatment group (Fig. 5b). For comparison, the decrease in  $SUV_{max}$  and pHe was not significant between Day –1 and Day 1, indicating that metformin required more than 1 day to affect tumor metabolism (Fig. 5c). A significant decrease in  $SUV_{max}$  was observed between day –1 and day 7 in the control group (Fig. 5a). This result suggested that the mice were affected by the handling and imaging scan sessions during the 9 days of the study, leading to lower glucose uptake in the tumor.

The average  $SUV_{max}$  and pHe of the tumors were not significantly different between metformin-treated and control groups at the start of the study, as anticipated (Table S1). However,  $SUV_{max}$  and pHe were also not significantly different between the two groups of mice on day 1 or day 7, raising concerns that these individual imaging biomarkers each failed to distinguish treatment from control. This result was particularly concerning for the study of pHe, because this result differed from the longitudinal change in tumor pHe that was significant for the treatment group but not for the control group. This lack of significant differences between the two groups on day 7 once again suggested that the mice were affected by the handling and imaging scan sessions during the 9 days of the study, which complicated the evaluation of treatment effects.

The same statistical analysis of the concentration of agent in the tumor showed a significant increase in agent concentration in the treated group between day –1 and day 7 (Fig. 5c and Table S1). A similar longitudinal change was not observed in the control group. This result suggested that metformin may have increased vascular perfusion in the tumor [27]. Similar to the results with the other imaging biomarkers, agent concentration was not significantly different between the two groups of mice on day –1 as anticipated, and yet the concentration was not significantly different between the two groups of mice on day 1 or day 7, so that concentration measurements failed to distinguish treatment from control.

We then evaluated the combination of  $SUV_{max}$  and pHe as synergistic biomarkers, using a Two-Sample Hotelling's  $T^2$  Distribution test (Table S1). This multivariate approach showed a significant change in the metformin-treated group from day –1 to day 7, further validating

that the PET and MRI biomarkers are sensitive to treatment response. More importantly, the control group did not show a significant longitudinal change based on this multivariate analysis. This result differed from evaluation of longitudinal changes in  $SUV_{max}$  for the control group that showed a significant decrease over time. This different result with multivariate analysis suggested that the handling and imaging scan sessions were insufficient to significantly change overall tumor metabolism, even though glucose uptake was affected. Most importantly, the multivariate analysis showed that the combination of  $SUV_{max}$  and pHe significantly differed between the treatment group and control group on day 7. This last result strengthened the assessment of metformin treatment, by showing a difference between treatment *vs.* control in addition to the longitudinal progression caused by treatment.

## Discussion

Simultaneous PET/MRI greatly facilitated our experimental design. In addition, no mice expired during our PET/MRI scan process (2 of 14 mice expired between imaging scans). In our previous attempt to perform this study with serial acidoCEST MRI followed by PET, six of eight mice expired during the transfer from the MRI instrument to the PET instrument or during the PET scan, and the two mice that survived were in poor physiological condition after the MRI and PET scans. This catastrophic loss during the serial study was attributed to the long sequential scan process, and additional handling and transport between MRI and PET scanning. Another serial PET and CEST MRI study was recently performed with shorter imaging protocols and a customized animal bed to facilitate transport, which demonstrated that serial PET and CEST MRI can be performed with care [28]. Yet as this other recent study indicated, maintaining the physiology of the mice is critical for studying drug effects on tumor metabolism, which is greatly facilitated by performing PET and MRI simultaneously. Other studies have demonstrated effects on mouse physiology due to prolonged anesthetic and *in vivo* imaging scans. Our studies reflect those previous observations by showing a decrease in  $SUV_{max}$  and pHe in the untreated control mice [29–31].

Our simultaneous PET/MRI study showed that PET or MRI could not individually differentiate drug-treated and control mice after initiating treatment. However, the simultaneous combination of the two imaging modalities could differentiate the two test groups 7 days after treatment was started. Furthermore, the combination of PET and MRI could detect a longitudinal change in the treated group that was not significantly present in the control group. As an additional benefit, the comparison of changes in  $SUV_{max}$  and pHe can provide greater insights regarding changes in cancer metabolism. In our study, the control group showed a longitudinal decrease in  $SUV_{max}$  without a significant decrease in pHe, which suggested that a change in glycolysis was not significant relative to an overall decrease in glucose uptake.

The therapeutic effects of metformin on tumor models in both mice and humans have been well studied [32, 33]. However, a decrease in tumor pHe after metformin treatment may seem counterintuitive, because a decrease in tumor metabolism would be expected to decrease lactic acid production, leading to an increase in tumor pHe. However, the observed decrease in tumor pHe can be explained by metformin's therapeutic mechanism. Metformin



inhibits the mitochondrial glycerophosphate shuttle that normally increases  $\text{NAD}^+$  concentration in the cytosol, which is used by lactate dehydrogenase B in the cytosol to convert lactic acid to glucose during gluconeogenesis [34]. Therefore, metformin indirectly inhibits the consumption of lactic acid in the cytosol, which leads to a decrease in tumor pHe [35]. While the observed decrease in tumor pHe provided evidence for the mechanistic effects of metformin, the decrease in tumor pHe could have been erroneously interpreted as an overall increase in tumor metabolism after treatment with metformin. Therefore, [ $^{18}\text{F}$ ]FDG PET analysis was critical for validating an overall decrease in tumor metabolism, which strengthens the interpretation of the acidoCEST MRI results. This synergy during experimental interpretation shows an additional merit for employing simultaneous PET/MRI during small animal drug studies.

Our initial PET/MRI study was designed to investigate the merits of simultaneous measurements of  $\text{SUV}_{\text{max}}$  and pHe. Based on these promising results, future PET/MRI studies are warranted with larger experimental designs. In particular, the number of mice in our preliminary study could be increased, especially to provide for more robust multivariate statistical analyses. *Ex vivo* histopathology should be included to validate drug effects on tumor metabolism. The concentration of iopamidol in the tumor tissue could also be used as an additional multivariate biomarker, especially for anti-cancer treatments that are anticipated to change tumor vascular perfusion as well as metabolism. From a technical perspective, our initial PET/MRI study indicated that a higher concentration of [ $^{18}\text{F}$ ]FDG could be administered for PET studies, which may improve the precision of the  $\text{SUV}_{\text{max}}$  measurements. Overall, our initial study shows the merits of simultaneous PET/MRI for performing these future studies.

## Conclusions

Our results have demonstrated that [ $^{18}\text{F}$ ]FDG PET and acidoCEST MRI studies can be performed simultaneously. The combination of  $\text{SUV}_{\text{max}}$  and pHe measurements provided a stronger assessment of the response to metformin in a MIA PaCa-2 flank tumor model. In addition, the decrease in tumor pHe matched expectations based on the therapeutic mechanism of metformin, while the decrease in  $\text{SUV}_{\text{max}}$  matched expectations based on general therapeutic effect, providing a more insightful evaluation of the effect of metformin on tumor metabolism.

## Supplementary Material

Refer to Web version on PubMed Central for supplementary material.

## Acknowledgments

The authors thank Ms. Christine Howison for assistance with PET/MRI studies, and Dr. Neale Hanke for assistance in preparing the tumor model. This research was supported by NIH grants R01 CA167183 and P50 CA95060.

## References

1. Bos R, van der Hoeven JJ, van der Wall E, et al. Biologic correlates of (18)fluorodeoxyglucose uptake in human breast cancer measured by positron emission tomography. *J Clin Oncol.* 2002; 20(2):379–387. DOI: 10.1200/JCO.2002.20.2.379 [PubMed: 11786564]
2. de Langen AJ, van den Boogaart, Lubberink M, et al. Monitoring response to antiangiogenic therapy in non-small cell lung cancer using imaging markers derived from PET and dynamic contrast-enhanced MRI. *J Nuc Med.* 2011; 52(1):48–55. DOI: 10.2967/jnumed.110.078261
3. Guo J, Guo N, Lang L, Kiesewetter DO, Xie Q, Li Q, Eden HS, Niu G, Chen X. <sup>18</sup>F-alfatide II and <sup>18</sup>F-FDG dual-tracer dynamic PET for parametric, early prediction of tumor response to therapy. *J Nuc Med.* 2014; 55(1):154–160. DOI: 10.2967/jnumed.113.122069
4. Chen LQ, Pagel MD. Evaluating pH in the extracellular tumor microenvironment using CEST MRI and other imaging methods. *Adv Radiol.* 2015; 2015:206405. doi: 10.1155/2015/206405 [PubMed: 27761517]
5. Chen LQ, Howison CM, Jeffery JJ, Robey IF, Kuo PH, Pagel MD. Evaluations of extracellular pH within in vivo tumors using acidoCEST MRI. *Magn Res Med.* 2014; 72(5):1408–1417. DOI: 10.1002/mrm.25053
6. Chen LQ, Randtke EA, Jones KM, Moon BF, Howison CM, Pagel MD. Evaluations of tumor acidosis within in vivo tumor models using parametric maps generated with acidoCEST MRI. *Mol Imaging Bio.* 2015; 17(4):488–496. DOI: 10.1007/s11307-014-0816-2 [PubMed: 25622809]
7. Jones KM, Randtke EA, Yoshimaru ES, et al. Clinical translation of acidosis measurements with acidoCEST MRI. *Mol Biol Imaging.* 2016; 19:617–626.
8. Longo DL, Dastru W, Digilio G, et al. Iopamidol as a responsive MRI-chemical exchange saturation transfer contrast agent for pH mapping of kidneys: in vivo studies in mice at 7 T. *Magn Reson Med.* 2011; 65(1):202–211. DOI: 10.1002/mrm.22608 [PubMed: 20949634]
9. Delli Castelli D, Ferrauto G, Cutrin JC, Terreno E, Aime S. In vivo maps of extracellular pH in murine melanoma by CEST-MRI. *Magn Reson Med.* 2014; 71(1):326–332. DOI: 10.1002/mrm.24664 [PubMed: 23529973]
10. Longo DL, Sun PZ, Consolino L, Michelotti FC, Uggeri F, Aime S. A general MRI-CEST ratiometric approach for pH imaging: demonstration of in vivo pH mapping with iobitridol. *J Am Chem Soc.* 2014; 136(41):14333–14336. DOI: 10.1021/ja5059313 [PubMed: 25238643]
11. Rancan G, Casstelli DD, Aime S. MRI CEST at 1T with large  $\mu_{\text{eff}}$  Ln<sup>3+</sup> complexes Tm<sup>3+</sup>-HPDO3A: an efficient MRI reporter. *Magn Reson Med.* 2016; 75(1):329–336. DOI: 10.1002/mrm.25589 [PubMed: 25651986]
12. Chen MM, Chen CY, Shen ZW, et al. Extracellular pH is a biomarker enabling detection of breast cancer and liver cancer using CEST MRI. *Oncotarget.* 2017; 8(28):45759–45767. DOI: 10.18632/oncotarget.17404 [PubMed: 28501855]
13. Akhenblit PJ, Hanke NT, Gill A, et al. Assessing metabolic changes in response to mTOR inhibition in a mantle cell lymphoma xenograft model using acidoCEST MRI; *Mol Imaging* 2016 29
14. Akhenblit PJ, Howison CM, Pagel MD. Assessing changes in tumor extracellular pH during metabolism-targeting therapies with acidoCEST MRI. *Proc WMIC.* 2015:576.
15. Anemone A, Consolin L, Conti L, et al. In vivo evaluation of tumor acidosis for assessing the early metabolic response and onset of resistance to dichloroacetate by using magnetic resonance pH imaging. *Int J Oncol.* 2017; 51(2):498–506. DOI: 10.3892/ijo.2017.4029 [PubMed: 28714513]
16. Chen LQ, Howison CM, Spier C, Stopeck AT, Malm SW, Pagel MD, Baker AF. Assessment of carbonic anhydrase IX expression and extracellular pH in B-cell lymphoma cell line models. *Leuk Lymphoma.* 2015; 56(5):1432–1439. DOI: 10.3109/10428194.2014.933218 [PubMed: 25130478]
17. Aime S, Calabi L, Biondi L, de Miranda M, Ghelli S, Paleari L, Rebaudengo C, Terreno E. Iopamidol: exploring the potential use of a well-established x-ray contrast agent for MRI. *Magn Reson Med.* 2005; 53(4):830–834. DOI: 10.1002/mrm.20441 [PubMed: 15799043]
18. Moon BF, Jones KM, Chen LQ, Liu P, Randtke EA, Howison CM, Pagel MD. A comparison of iopromide and iopamidol, two acidoCEST MRI contrast media that measure tumor extracellular

- pH. *Contrast Media Mol Imaging*. 2015; 10(6):446–455. DOI: 10.1002/cmimi.1647 [PubMed: 26108564]
19. Ward KM, Aletras AH, Balaban RS. A new class of contrast agents for MRI based on proton chemical exchange dependent saturation transfer (CEST). *J Magn Reson*. 2000; 143(1):79–87. DOI: 10.1006/jmre.1999.1956 [PubMed: 10698648]
  20. Judenhofer MS, Wehrli HF, Newport DF, Catana C, Siegel SB, Becker M, Thielscher A, Kneilling M, Lichy MP, Eichner M, Klingel K, Reischl G, Widmaier S, Röcken M, Nutt RE, Machulla HJ, Uludag K, Cherry SR, Claussen CD, Pichler BJ. Simultaneous PET-MRI: a new approach for functional and morphological imaging. *Nat Med*. 2008; 14(4):459–465. DOI: 10.1038/nm1700 [PubMed: 18376410]
  21. Goertzen AL, Stortz G, Thiessen JD, et al. First results from a high-resolution small animal SiPm PET insert for ET/MR imaging at 7T. *IEEE Trans Nucl Med*. 2016; 85:22424–22433.
  22. Shah T, Lu L, Dell KM, Pagel MD, Griswold MA, Flask CA. CEST-FISP: a novel technique for rapid chemical exchange saturation transfer MRI at 7T. *Magn Reson Med*. 2011; 65(2):432–437. DOI: 10.1002/mrm.22637 [PubMed: 20939092]
  23. Stortz G, Thiessen JD, Bishop D, Khan MS, Kozłowski P, Retière F, Schellenberg G, Shams E, Zhang X, Thompson CJ, Goertzen A, Sossi V. Performance of a PET insert for high resolution small animal PET/MR imaging at 7T. *J Nucl Med* 2017 jnumed.116.187666.
  24. Thiessen JD, Shams E, Stortz G, Schellenberg G, Bishop D, Khan MS, Kozłowski P, Retière F, Sossi V, Thompson CJ, Goertzen AL. MR-compatibility of a high-resolution small animal PET insert operating inside a 7 T MRI. *Phys Med Biol*. 2016; 61(22):7934–7956. DOI: 10.1088/0031-9155/61/22/7934 [PubMed: 27779126]
  25. Sheth VR, Liu G, Li Y, Pagel MD. Improved pH measurements with a single PARACEST MRI contrast agent. *Contrast Media Molec Imaging*. 2012; 7(1):26–34. DOI: 10.1002/cmimi.460 [PubMed: 22344877]
  26. Jones KM, Randtke EA, Howison CM, Pagel MD. Respiration gating and Bloch fitting improve pH measurements with acidoCEST MRI in an ovarian orthotopic tumor model. *Proc SPIE Int Soc Opt Eng*. 2014; 9788:978815. doi: 10.1117/12.2216418
  27. Triggle CR, Ding H. Metformin is not just an antihyperglycaemic drug but also has protective effects on the vascular endothelium. *Acta Physiol*. 2017; 219(1):138–151. DOI: 10.1111/apha.12644
  28. Longo DL, Bartoli A, Consolino L, Bardini P, Arena F, Schwaiger M, Aime S. In vivo imaging of tumor metabolism and acidosis by combining PET and MRI-CEST pH imaging. *Cancer Res*. 2016; 76(22):6463–7470. DOI: 10.1158/0008-5472.CAN-16-0825 [PubMed: 27651313]
  29. Hildebrandt JJ, Su H, Weber WA. Anesthesia and other considerations for in vivo imaging of small animals. *ILAR J*. 2008; 49(1):17–26. DOI: 10.1093/ilar.49.1.17 [PubMed: 18172330]
  30. Wolf G, Abolmaali N. Imaging tumour-bearing animals using clinical scanners. *Int J Radiat Biol*. 2009; 85(9):752–762. DOI: 10.1080/09553000902954520 [PubMed: 19479601]
  31. Lukasik VM, Gillies RJ. Animal anesthesia for in vivo magnetic resonance. *NMR Biomed*. 2003; 16(8):459–467. DOI: 10.1002/nbm.836 [PubMed: 14696002]
  32. Yousef M, Tsiani E. Metformin in lung cancer: review of in vitro and in vivo animal studies. *Cancers Cancers (Basel)*. 2017; 9(5):E45. doi: 10.3390/cancers9050045 [PubMed: 28481268]
  33. Lonardo E, Cioffi M, Sancho P, et al. Metformin targets the metabolic achilles heel of human pancreatic cancer stem cells. *PLoS One*. 2013; 8(10):e76518. doi: 10.1371/journal.pone.0076518 [PubMed: 24204632]
  34. Yeon K, Lee MS. New mechanisms of metformin action: focusing on mitochondria and the gut. *J Diabetes Investig*. 2015; 6:600–609.
  35. DeFronzo R, Fleming AG, Chen K, Bicsak TA. Metformin-associated lactic acidosis: current perspectives on causes and risk. *Metab Clin Exp*. 2015; 65:20–29. [PubMed: 26773926]

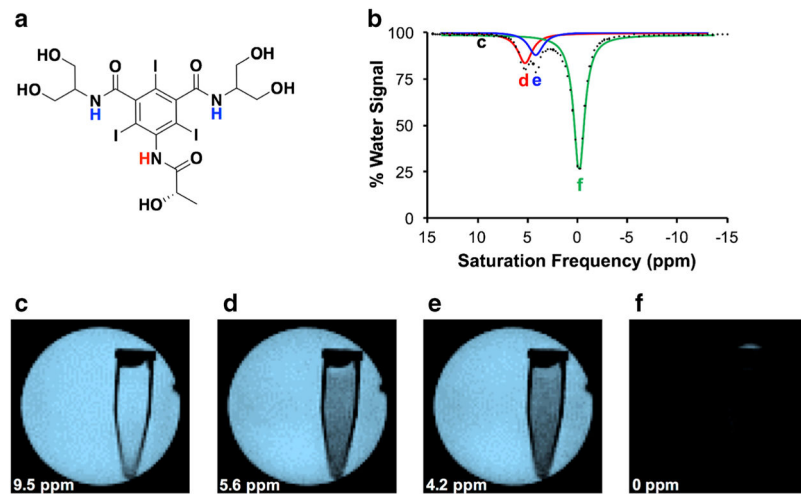


**Fig. 1.** The acidoCEST MRI method. **a** Iopamidol has one amide proton that resonates at 5.6 ppm (red) and two magnetically equivalent amide protons that resonate at 4.2 ppm (blue), relative to the water resonance defined as 0 ppm. **b** A CEST spectrum of 20 mM of iopamidol in water shows a decrease in % water signal when saturation is applied at 5.6 or 4.2 ppm, as well as the direct saturation of water when saturation is applied at 0 ppm. The labels c–f show saturation frequencies used to produce panels c–f. **c–f** MR images of water signal in a tube of 20 mM iopamidol in a larger tube of water, with saturation applied at 9.5, 5.6, 4.2, and 0 ppm.

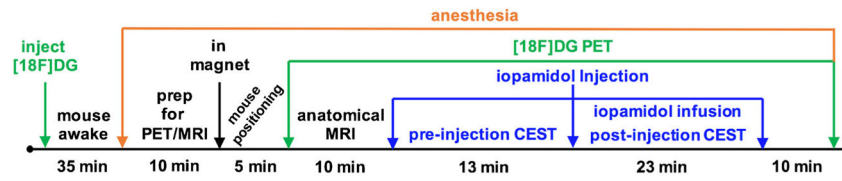


**Fig. 2.**  
A schematic of the PET/MR imaging workflow.

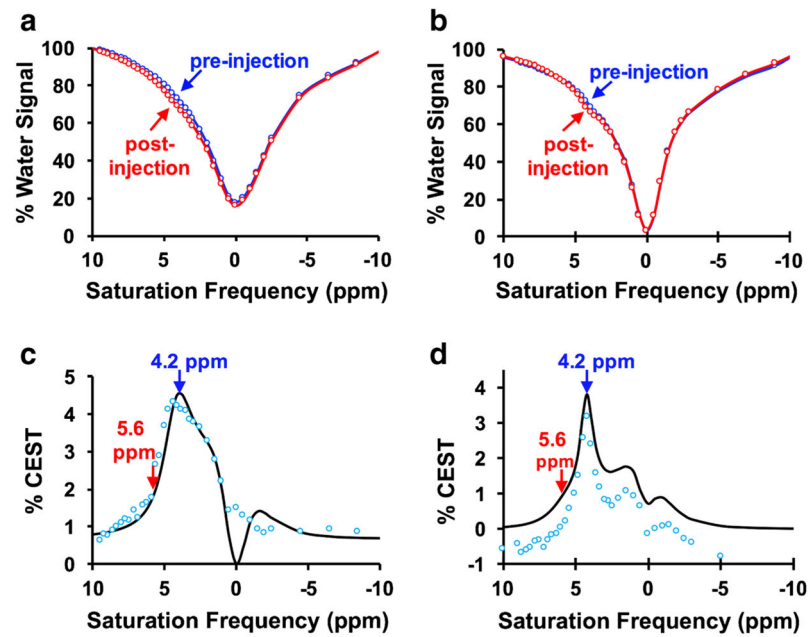


**Fig. 3.** *In vivo* CEST spectra. The post-injection spectrum shows lower % water signal than the pre-injection spectrum at 4.2 and 5.6 ppm, for **a** a tumor with pHe 7.0, and **b** a tumor with pHe 6.8. **c** The difference between pre-injection and post-injection CEST spectra (blue circles) were fit with the Bloch-McConnell equations modified for chemical exchange (black line) for a tumor with pHe 7.0, and **d** a tumor with pHe 6.8.

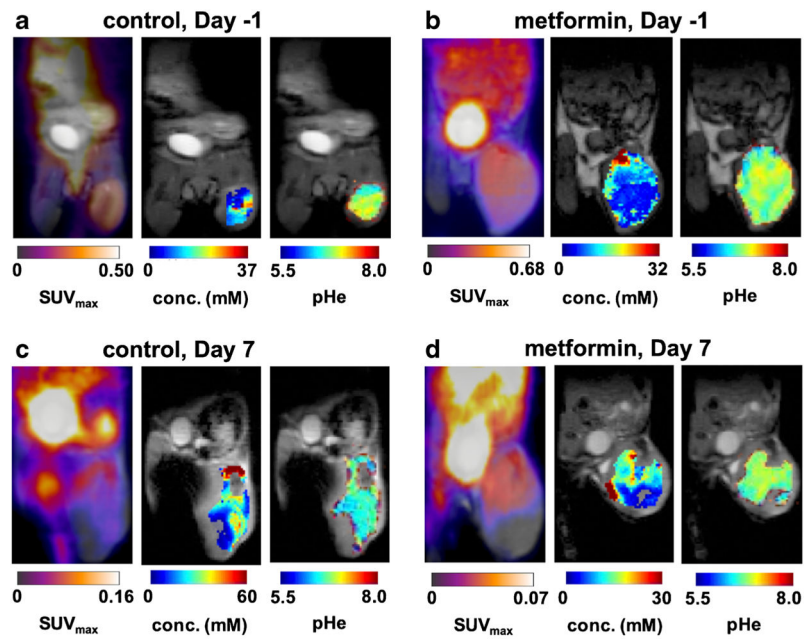


**Fig. 4.** PET/MR images. **a** Images are shown for MIA PaCA-2 tumor model 1 day before treatment with metformin, **b** 1 day before treatment with vehicle control, **c** 7 days after treatment with metformin, and **d** 7 days after treatment with vehicle control. SUV<sub>max</sub> maps of [<sup>18</sup>F]FDG show high signal in the flank tumor in the right leg. Very high signal was detected in the bladder. Parametric maps of iopamidol concentration and pHe in the tumor are overlaid on an anatomical MR image.

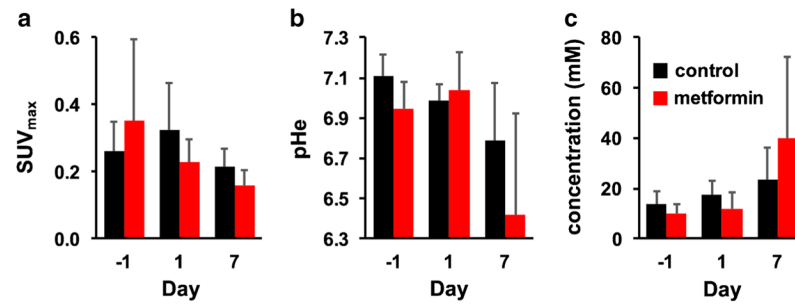


**Fig. 5.**

The effect of metformin on imaging biomarkers. **a**  $SUV_{max}$  measured with [ $^{18}F$ ]FDG PET showed a significant decrease ( $p = 0.05$ ) in the metformin-treated group and in the control group with longitudinal imaging.  $SUV_{max}$  was not significantly different ( $p > 0.05$ ) between the metformin-treated and control groups on day 7. **b** pHe also significantly decreased in the metformin-treated group, but the decrease in pHe in the control group was not significant. pHe was not significantly different between the metformin-treated and control groups on day 7. **c** The concentration of iopamidol in the tumor significantly increased in the metformin-treated group, but did not significantly increase in the control group. Iopamidol concentrations were not significantly different between the metformin-treated and control groups on day 7.